A review of electronic portal imaging devices (EPIDs)

Arthur L. Boyer
Department of Radiation Physics, The University of Texas, M. D. Anderson Cancer Center, Houston, Texas 77030

Larry Antonuk
Department of Radiation Oncology, University of Michigan Medical Center, Ann Arbor, Michigan 48109

Aaron Fenster
J. P. Robarts Research Institute, 100 Perth Drive, London, Ontario N6A 5K8, Canada

Marcel Van Herk and Harm Meertens
The Netherlands Cancer Institute, Antoni van Leeuwenhoek Huis, Plesmanlaan 121, 1066 CX, Amsterdam, The Netherlands

Peter Munro
London Regional Cancer Centre, 790 Commissioner's Road East, London, Ontario N6A 4L6, Canada

Larry E. Reinstein
University Hospital at Stony Brook, Department of Radiation Oncology, Stony Brook, New York 11794-7028

John Wong
Mallinckrodt Institute of Radiology, 510 S. Kingshighway Boulevard, St. Louis, Missouri 63110

On-line electronic portal imaging devices are beginning to come into clinical service in support of radiotherapy. A variety of technologies are being explored to provide real-time or near real-time images of patient anatomy within x-ray fields during treatment on linear accelerators. The availability of these devices makes it feasible to verify treatment portals with much greater frequency and clarity than with film. This article reviews the physics of high-energy imaging and describes the operation principles of the electronic portal imaging devices that are under development or are beginning to be used clinically.

I. INTRODUCTION

The importance of the placement of treatment portals to achieve local tumor control is intuitively obvious and objectively documented.[1,2] Uncertainty in the localization of field margins in general practice is difficult to estimate,[3-6] but random positioning precision has been measured with one standard deviation in the neighborhood of 10 to 20 mm. It has been estimated that systematic discrepancies between actual radiation field edge positions and intended or planned positions should in general be less than about 5 mm.[7] The day to day variation in field edge position should occur with a standard deviation below about 2 mm. The principal technical advance in the last 2 decades to improve portal localization was the development of specialized film emulsions whose sensitivities were appropriate for radiotherapy.[8] Methods to enhance these films by image processing were a logical but time-consuming adjuvant for this technique.[9-11] However, during the last few years rather intensive efforts have led to the development of techniques that produce images using high-energy x rays directly.[12,13] As a result, electronic portal imaging devices (EPIDs) are becoming available to cancer radiotherapy. In some systems, a small fraction of the radiation dose delivered on a given day can be used to produce a digital on-line image that is displayed in real time or near real time. These imaging systems enable treatment beam alignment to be visualized with respect to patient anatomy before a full radiation dose is administered. If developed sufficiently, such systems may provide a practical means to control field margin placement to within the 5-mm goal.

This review has two major purposes: First, to examine some of the limitations of imaging with high-energy radiation beams, and second, to review the EPIDs that are currently being developed for clinical use. A wide variety of radiation detection and optoelectronic techniques have been used to produce EPIDs. Here, we review several optical systems that direct x-ray-induced fluorescence onto a video camera, and several scanning techniques that employ liquid ionization chambers, photodiodes, or other solid-state devices. We seek to provide a simple description of each device in terms of the theory of imaging and the underlying physical processes at work.

It is important for medical physicists and other personnel providing technical support for radiotherapy to understand this emerging technology. As these devices become available commercially, EPIDs must be specified, tested, accepted, and commissioned. One will need to select specific devices that meet specific clinical goals and to devise practical tests to determine whether the desired specifications have been met. Thus it is important to identify system performance parameters and their relevance to image quality. Although

typical achievable ranges of performance parameters will be described here, this paper will not attempt to compare the performance parameters of the EPID technologies. Indeed, EPIDs are still maturing too rapidly for meaningful comparisons to be made. Instead, the ground work for such comparisons will be laid so that future workers can make comparisons under the appropriate circumstances.

II. RADIOGRAPHIC IMAGING PERFORMANCE

A. Theoretical performance

The limitations of imaging with high-energy radiation beams can be established, at least partially, using the formalism developed by Motz and Danos[14] for their analysis of diagnostic imaging systems. In their approach, the detectability of a small anatomic structure embedded within a homogeneous body is determined. The analysis is restricted so that only subject contrast, statistical noise, and x-ray scatter influence the estimation of the signal-to-noise ratio (SNR).[14]

We will consider an idealized imaging situation in which x rays pass through a homogeneous medium of uniform thickness L having attenuation coefficient μ. On average, some photons are attenuated in the medium, some photons exit the medium without interacting at all, and a number n_s scatter in the medium and yet are detected exiting the medium. On average, $n = n_T$ x-ray quanta are detected as an image background of which a fraction $F = n_s/n_T$, known as the scatter fraction, have been scattered.

Embedded within the homogeneous medium there is an anatomic structure having attenuation coefficient μ_x and thickness L_x such that n' total x-ray quanta are detected behind the anatomic structure. Subject contrast is defined as the ratio of the signal difference between the anatomic structure and the background, to the mean carrier signal. Therefore, subject contrast in this case can be expressed as

$$S = 2[(n - n')/(n + n')].   (1)$$

Equation (1) can be rewritten as[14]

$$S = \frac{2(1 - e^{-\Delta})}{[1 + e^{-\Delta} + (2 \cdot F)/(1 - F)]},   (2)$$

where $\Delta = L_x(\mu_x - \mu)$ represents the difference in attenuation between the anatomic structure and the background. Equation (2) shows that subject contrast increases if the difference in attenuation between the anatomic structure and the background (Δ) increases, or if the scatter fraction (F) decreases.

The most important parameter that determines the image information content is the signal-to-noise ratio (SNR). The SNR is given by the ratio of the signal difference between an anatomic structure and its background to the statistical noise associated with detection of the x-ray quanta necessary to form this signal difference. Hence, SNR can be written as

$$SNR = (n - n')/\sqrt{n + n'},   (3)$$

where n and n' have the same meaning as defined in Eq. (1). Motz and Danos[14] have shown that the SNR can be rewritten as

$$SNR = \left[A\Phi\eta e^{-\mu L}\left(1 + e^{-\Delta} + \frac{2F}{1 - F}\right)\right]^{1/2} \cdot \frac{S}{2},   (4)$$

where A is the area of the anatomic structure of interest, Φ is the photon fluence impinging on the patient, η is the x-ray quantum efficiency of the detector, and S is the subject contrast defined in Eq. (2). Equation (4) predicts that the SNR will increase as the size of the structure of interest increases, the subject contrast S increases, or, the number of x-ray quanta used to form the image increases.

The above equations can be used to analyze the limitations of imaging with high-energy radiation beams. The subject contrast for a 1-cm-thick cortical bone structure embedded in a 20-cm-thick body of water, as a function of monoenergetic beam energy, is plotted in Fig. 1. These results have been calculated using the attenuation coefficients for bone, air, and water found in Appendix A of Johns and Cunningham[15] and by extrapolating the scatter fraction data measured by Motz and Dick.[16] The scatter fractions, which vary from 0.4 to 0.5, are for a 25-cm-diam beam with no air gap between the patient and the detector. It is clear from Fig. 1 that one of the major limitations of imaging with high-energy radiation beams is the low subject contrast. The subject contrast for the bony object is 18.5% when irradiated by a 50-keV x-ray beam; however, it drops to 1.8%, 1.4%, and 1.0% when irradiated by 1.25-, 2-, and 6-MeV radiation beams, respectively. Subject contrast is 10–20 times less at radiotherapy energies than at diagnostic energies.

Much larger numbers of x-ray quanta interact with the radiation detector when forming a radiotherapy image, which partly compensates for the low subject contrast at higher x-ray energies. There are a number of reasons why larger numbers of x-ray quanta reach the detector in portal imaging. Much larger doses are delivered to a patient during a radiotherapy treatment than is considered acceptable in diagnostic radiology, resulting in a much larger photon fluence impinging on the patient. The high-energy radiation
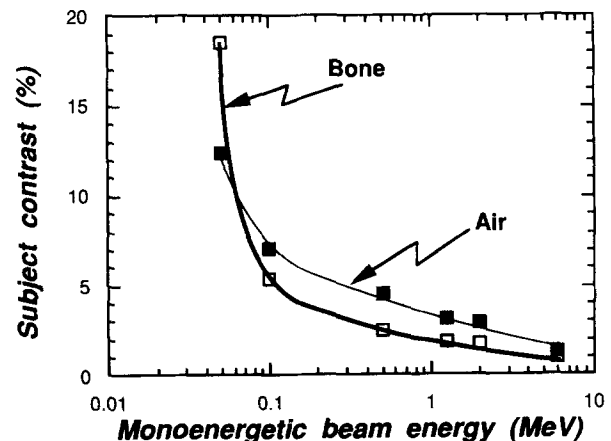

FIG. 1. Subject contrast as a function of monoenergetic beam energy for a 1-cm bony structure and a 1-cm air cavity embedded in a 20-cm-thick water medium. The calculations assumed a 25-cm-diam beam and no air gap between the patient and the detector. Bone is represented by the open symbols and air by the solid symbols.
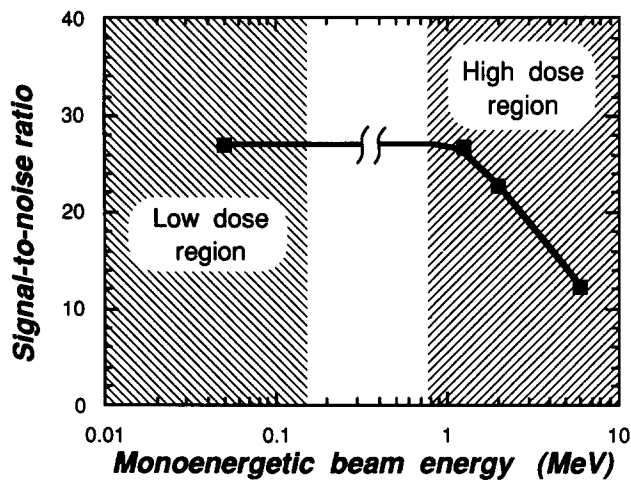
FIG. 2. The SNR to be expected for a 1-cm bony object embedded in a 20-cm-thick water medium when using exposures typical for diagnostic radiology (low dose region) and for radiation therapy (high dose region). The calculations assume the same geometry as in Fig. 1. The calculations assume that the typical dose for a diagnostic radiograph is 0.05 cGy, while the typical radiation dose for a radiotherapy image is 10 cGy.
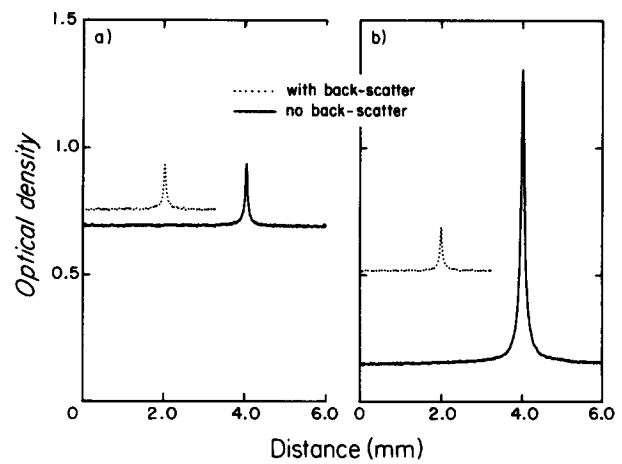

FIG. 3. Line spread functions (LSFs) measured using tungsten blocks that formed slits that were: (a) 25 and (b) 105 mm deep. The figure illustrates the effect of backscatter on the LSF measurements, which were done using film. LSFs produced under conditions that maximize scatter (large field size, blocks close to a wall) are indicated by dotted lines, while those produced under conditions that minimize scatter are indicated by solid lines. The tails of the solid curve in (b) are close to base plus fog optical densities, indicating that little radiation penetrates the thick tungsten blocks.

is much more penetrating so that a larger fraction of the radiation exits from the patient. In addition, primary x-ray quanta are not attenuated in grids, as in diagnostic radiology. All of these factors result in a much greater photon fluence reaching the radiation detector in a radiotherapy beam and in increased SNR [see Eq. (4)].

Since the dose required to form a portal image can be measured, the photon fluence associated with these exposures can be calculated using the fluence-to-dose conversion tables calculated by Rogers.[17] In turn, the photon fluence can be used [see Eq. (4)] to calculate the SNR for a 1-cm bony object as a function of monoenergetic beam energy. In Fig. 2 are plotted the SNRs expected when forming images with the typical doses used in diagnostic radiology (0.05 cGy) and radiation therapy (10 cGy). The surprising result is that the SNR does not drop precipitously as the energy of the radiation beam increases from diagnostic to radiotherapy energies. According to the simple model of Motz and Danos, the increased number of x-ray quanta used to form the radiotherapy image compensates for any loss in subject contrast as the energy of the radiation beam increases. The model predicts that the 1-cm bony object should be equally detectable when irradiated by 50-keV or 1.25-MeV radiation beams, as long as sufficient number of x-ray quanta are used at the higher energy to compensate for the loss in subject contrast.

Unfortunately, the model of Motz and Danos does not account for loss of spatial resolution or system noise. The only way to determine what effect these quantities have on the image performance is to quantitatively evaluate the spatial resolution, noise, and signal-to-noise properties of portal imaging systems.

B. Spatial resolution

Spatial resolution or the signal transfer properties of a radiation detector can be characterized by the detector's

modulation transfer function MTF (f).[18] The technique used to measure the MTF(f) of x-ray detectors irradiated by radiotherapy beams has been described by Droege et al.[19] and Munro et al.[20,21] and is based on the techniques described by Doi et al.[18] In brief, the experimental approach is to produce a very narrow radiation beam using large collimators that form a small (25- to 50-μm) gap. The response of the radiation detectors to the narrow radiation beam, which is known as the line spread function (LSF), is determined by the spread of the signal in the detector. The modulus of the Fourier transform of the detector's normalized LSF gives the MTF (f).

One major difference between measuring MTF (f)'s using radiotherapy x-ray beams compared with diagnostic x-ray beams is that scattered radiation from the collimators forming the slit is a much larger problem. Care must be taken to ensure that the signal recorded by the detector is due to radiation passing through the slit and not radiation scattered out of the side of the collimators and then backscattered from the walls, ceiling, or floor.[20] Figure 3 shows how this scatter can influence the measured LSFs. Some typical LSFs for a tungsten plate irradiated by ^{60}Co and 18-MV radiation beams are shown in Fig. 4.[20] The LSFs show that the spread in the tungsten plate is due to (i) lateral migration of electrons, which leads to the large peak close to the slit; and (ii) photons scattered in the detector, which create the long tails in the LSFs. These results are similar to these for copper and lead plates and thus are representative of the spatial resolution that could be expected for portal films.[14]

C. Noise

The noise transfer properties of an x-ray detector can be characterized by the detector's noise power spectrum, or NPS(f). The mean-square departure of signal from its aver-
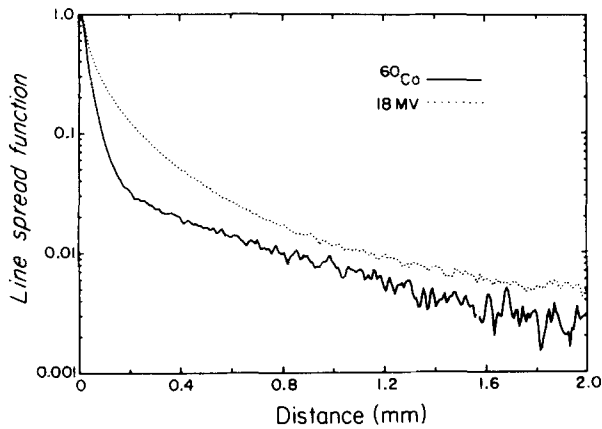
FIG. 4. Line spread function (LSFs) for a 1.5-mm-thick tungsten plate irradiated by ^{60}Co and 18-MV radiotherapy beams.

age value is the variance, and the analysis of these fluctuation into spatial frequency components gives the noise power spectrum.[18] In diagnostic x-ray imaging, the total noise power is considered to be due to components which are statistically independent of each other: such as (i) quantum noise, caused by statistical fluctuations in the number of x-ray quanta interacting with the detector; and (ii) system (e.g., film) noise. Munro *et al.*[20] have shown that film noise in portal films accounts for 50%–90% of the total noise power. Therefore, one reason why the predictions of the Motz and Danos model do not correlate with the commonly accepted wisdom about the image quality of portal films, is because the model does not take into account the large amount of film noise. The model of Motz and Danos and the NPS(f) results of Munro *et al.*[20,22] suggest that portal images of much higher quality than current portal films can be obtained.

D. Detective quantum efficiency

The most important physical quantity that must be determined is the signal-to-noise property of the imaging systems. The detective quantum efficiency, or DQE(f), gives the SNR^2 transfer characteristics of an imaging system as a function of spatial frequency. Consider a system for which SNR$_{in}$ (f) is the input SNR and SNR$_{out}$ (f) is the output SNR. Then the DQE produced by the imaging system is defined as[18,23]

$$DQE(f) = [SNR_{out}(f)/SNR_{in}(f)]^2. \quad (5)$$

The DQE(f) gives a measure of how efficient the imaging system is at transferring SNR (i.e., information) contained in the radiation beam. Equation (5) can be rewritten[18,23,24]

$$DQE(f) = (K)^2 MTF^2(f)/\Phi NPS(f), \quad (6)$$

where K is a constant that takes into account the response (i.e., gain) of the imaging system to radiation exposure. For a digital imaging system, where the response of the system is directly proportional to exposure, $K = $ unity. The DQE(f), which gives a measure of how efficiently the imaging system makes use of the radiation (i.e., image information), is re-

duced if the imaging system causes a loss of spatial resolution [reduces the MTF(f)], adds system noise [increases NPS(f)], or does not efficiently detect all of the x-ray quanta impinging on it.

In diagnostic radiology, the aim is to maximize the DQE(f) of an imaging system so that a high-quality image can be acquired while minimizing patient exposure. A similar aim is important in radiation therapy. Since the treatment beam is used to form the image, the patient exposure must be kept small in case field-placement errors occur. Furthermore, as treatment techniques such as conformal radiotherapy and hyperfractionation (which reduce the dose per treatment field) become more common, there will be increasing demands on the portal imaging systems to form high-quality images with small (e.g., 1 cGy) exposures. Therefore, as in diagnostic radiology, imaging systems with high DQE(f) will be required for portal imaging.

Figure 5 shows the DQE(f) for a 400 mg/cm^2 layer of gadolinium oxysulfide (Gd$_2$O$_2$S) phosphor bonded to a copper plate, when irradiated by ^{60}Co, 6- and 18-MV radiation beams.[21] For an ideal detector, with no secondary quantum statistical contributions, the DQE(f) at zero spatial frequency is equal to the x-ray quantum efficiency of the radiation detector. For these radiation beams and the metal plate radiation detectors the x-ray quantum efficiency is less than 2%. The x-ray quantum efficiency of the metal plate/phosphor screen combination is low, since only 5% to 7% of the radiation impinging on the detector is attenuated, and since only a fraction of the x-ray interactions results in electrons that cause scintillation in the phosphor.

The low x-ray quantum efficiency of the detector shown in Fig. 5 has implications for almost all of the portal imaging systems described in this review. All but one of the portal imaging systems (the exception is the "crystal array" being developed by Swindell and his colleagues) employ a metal plate as their x-ray detector. These imaging systems differ only in the type of recording device (e.g., scintillating phosphors, liquid ionization chambers, diode arrays) used to interact with the high-energy electrons emitted by the metal
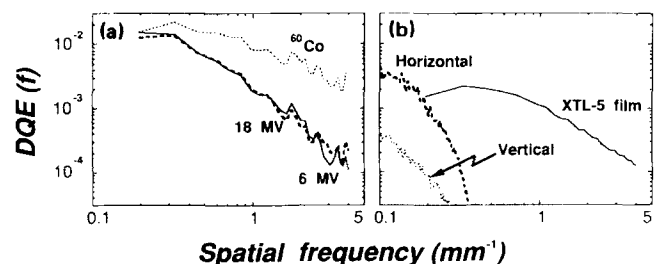

Spatial frequency (mm^{-1})

FIG. 5. The detective quantum efficiency DQE(f) for a copper plate combined with a 400-mg/cm^2 phosphor screen when irradiated by ^{60}Co, 6- and 18-MV radiation. (a) The DQE(f) for the metal plate/phosphor detector alone. (b) The DQE(f) of the entire detector system consisting of the plate/phosphor, the optical lens, and the vidicon TV camera, measured when irradiated by a 6-MV beam. The DQE(f) of XTL-5 radiographic film in contact with a tungsten plate 1.5 mm thick (3.0 g/cm^2)[14] is also plotted in (b).

plate. Therefore, the maximum DQE(f) for all of the portal imaging systems is determined by the metal plate, which at low spatial frequencies should be similar to that shown in Fig. 5. The results shown in Fig. 5 also suggest that there is much more information in the radiotherapy beam than is detected by the metal plate detectors. This fact holds promise for future portal imaging systems that may far outperform those described in this review.

E. Contrast-resolution evaluation

A less complete but operationally simpler way to characterize the performance of an imaging system is by means of a contrast-resolution phantom. A test phantom has been developed for portal film evaluation[25] and is available commercially. Munro has described a contrast-resolution phantom[21] consisting of ten rows and ten columns of holes drilled into a 1.3-cm-thick aluminum block. The holes down each row vary in diameter from 12.8 to 1.19 mm and the holes along each column range in depth from 4.57 to 0.29 mm. This phantom provides a rapid means to evaluate and compare portal imaging systems, when the phantom is used under identical geometric and exposure conditions. This phantom is also available commercially. (Constrast Detail Phantom, Radiation Measurements Inc., Middleton, Wisconsin.)

F. Other considerations

Almost all of the EPIDs manipulate the raw image pixels before they are displayed. Typically, if $p_{i,j}^*$ represents the raw pixel array, then there are at least two additional arrays that are used to process the image. First, there is usually a background array $b_{i,j}$ that is collected from the detector in the absence of radiation. Second, there is a flood-field image $f_{i,j}$ that contains radiation beam unflatness and variations in detector efficiency (e.g., nonuniformities in the light output of the phosphor screen) across the field of view. A corrected image $p_{i,j}$ is typically obtained by the operation,

$$p_{i,j} = (p_{i,j}^* - b_{i,j})/(f_{i,j} - b_{i,j}). \tag{7}$$

Additional system-dependent algorithms are required by the various imaging technologies. Both the background array ($b_{i,j}$) and the flood field image ($f_{i,j}$) will contain noise, since they are both images obtained from the portal imaging system. Thus the corrected image ($p_{i,j}$) will have more noise than the raw image ($p_{i,j}^*$), although structural nonuniformities (often call "structural noise") will be eliminated.

G. Summary

Conventionally, portal films have been considered to exhibit poor image quality. We have attempted to show that the poor image quality may be due to poor characteristics of the systems (i.e., metal plates and films) forming the images rather than any fundamental limitation in information content of high-energy radiation beams. We believe that much more information is contained in the radiation beams than is currently being extracted. The imaging systems described in the following sections are early attempts to extract more information from these high-energy beams.

III. IMAGING TECHNOLOGIES

A. Mirror-based video systems

The most common portal imaging systems are video-based systems that consist of a metal plate coated with a fluorescent phosphor screen viewed by a video camera with the aid of a front-surface 45° mirror as depicted in Fig. 6. X-ray interactions in the metal plate create high-energy electrons that in turn produce fluorescence in the phosphor screen. Only a small fraction of the light (0.01%) is collected by the lens,[26] so care must be taken in selecting components of the imaging system in order to maximize light collection efficiency of the optical chain. The video system has a number of advantages including: (i) the x-ray detector subtends the entire treatment field so that all of the x-ray quanta exiting from the patient can contribute to the image; (ii) the spatial resolution of the system can be high, depending upon the thickness of the phosphor screen; and (iii) the system can generate images quickly (at or close to 30 frames/s). A disadvantage of mirror video-based systems is that they must isolate a large optical path, making the devices bulky. Therefore, they can hamper patient setup and they cannot be used on treatment machines with beam stoppers. Nevertheless, the mirror systems, which are gantry mounted, use various designs to make the mirror and detector assembly demountable or collapsible to minimize interference with patient setup.

Because of their general availability, video cameras were used as early as 1958 to image therapy fields.[27–30] The first fluoroscopic imaging system specifically designed for megavoltage imaging that used what could be considered "modern" technology was reported by Baily and his colleagues in 1980.[12] Since then, many other investigators[31–34] have described systems that use a variety of metal plates, different thicknesses of phosphor screens, different types of video cameras, and video processing boards with different display and storage capabilities. For example, Leong used a silicon-intensified target (SIT) camera,[31] Shalev *et al.* used both intensified CCD and SIT cameras,[32] Visser *et al.* used a CCD camera with slow scan readout capabilities,[33] and Munro *et al.* used a lead oxide tube camera specially adapted to accumulate the video signal on the lead oxide target of the tube for lengthy periods.[26,34] The target accumulation described by Munro not only improved image quality by reducing video noise, but it also greatly simplified synchronization of image acquisition with patient irradiation.
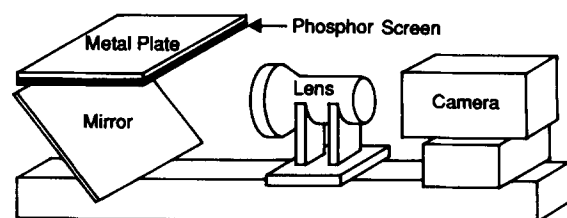

FIG. 6. Schematic of a video-based EPID consisting of a fluorescent phosphor attached to a metal plate, viewed by a video camera (fitted with an appropriate lens) using a 45° mirror.
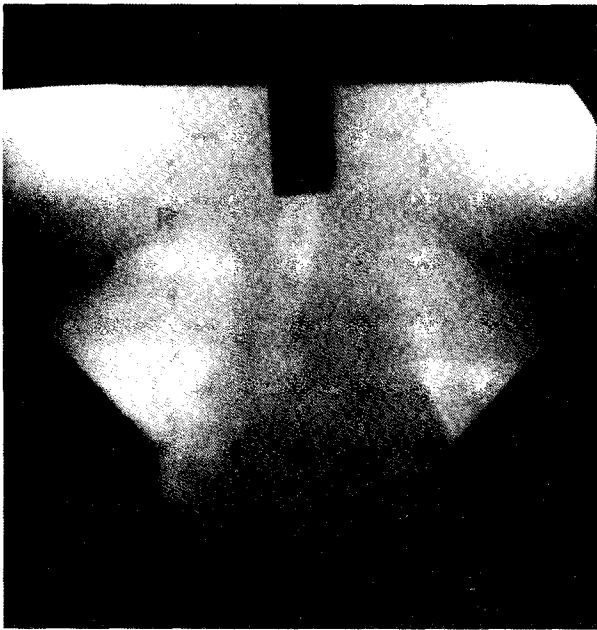
FIG. 7. An image produced by a mirror system (Munro and Fenster). Note the resolution of the trachea, lungs, and bony anatomy. The image was formed using a 6-MV irradiation of approximately 1.5 cGy at the isocenter.

Image quality has generally been good, and recent advances have demonstrated that high-quality images can be acquired using irradiations as short as 1–2 monitor units. An unpublished contrast-detail study (Las Vegas contrast-detail phantom study) comparing a number of mirror systems has shown that structures as small as 1 mm in diameter (5% primary subject contrast) and structures as low as 0.6% primary subject contrast (15 mm in diameter) can be detected. Thus mirror systems have demonstrated high spatial and contrast resolution. An example of an image produced by a mirror system is given in Fig. 7. Future improvements also appear likely. Munro *et al.*[21] have recently published some measurements quantitatively evaluating the performance of their video-based imaging system. Because of spatial resolu-

tion losses caused by the lens and additional noise added by the video camera and secondary light quanta, the DQE(f) of their system [Fig. 5(b)] is still lower than that for the metal plate/phosphor screen detector alone [Fig. 5(a)]. Therefore, improvements in video cameras and geometric optics should result in even higher image quality in the future.

One area for improvement is in the efficiency of the mirror systems' optics. The expression for ϵ_{lens}, the efficiency of a lens, is

$$\epsilon_{lens} = k\,[\tau M^2/(1+M)^2 f^2],\qquad(8)$$

where τ is the lens transmission factor (generally $\tau \approx 0.9$); M is the lens magnification factor, which is defined as size of the virtual image on the TV camera divided by the size of the image on the x-ray detector ($M \ll 1$); k is a factor equal to 1/16 when assuming each point on the phosphor screen is an isotropic point source irradiating into 4π steradians; and, f is the f-number (focal length/diameter) of the lens. With all other factors equal, the efficiency increases as the inverse square of the f/number, as one would expect. Increasing the size of the TV camera or light sensor will increase M, improve the efficiency of the mirror systems' optics, and should improve the DQE(f) of mirror systems. Thus plans to use TV cameras with larger format tubes, or large area charge-coupled devices (CCDs) should improve image quality further.

B. Fiber-optic video systems

Although excellent portal images can be acquired with mirror-based EPIDs, the presence of the large mirror introduces implementation problems, as mentioned previously, in many treatment geometries. Replacing the mirror with a two-dimensional array of fiber-optic image reducers has been demonstrated.[35,36] Several prototype fiber-optic systems have been constructed to operate as depicted in Fig. 8. X rays produce light by fluorescence at the input of the device. A 1.5-mm copper metal sheet provides electron build-up. Fluorescence occurs in a layer of gadolinium oxysulfide phosphor 250–500 mg/cm^2 thick. The fiber-optic channels
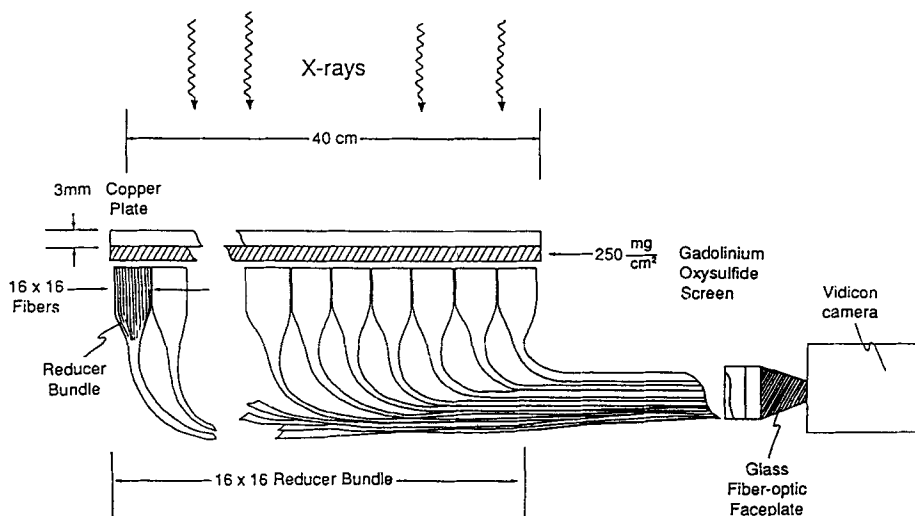

FIG. 8. Schematic of a fiber-optic EPID consisting of a fluorescent phosphor on a metal plate, a fiber-optic light channel device to direct light to a video camera.

consist of clear polystyrene columns 1.6×1.6 mm encased by a thin acrylic cladding. The difference in the refractive indices between the two plastics allow for "light piping," providing that the angle of the incident light satisfies the condition of total internal reflection at the cladding interface.

The next larger subunit is a "multi-fiber" reducer consisting of 16×16 individual columns which each reduce to a 0.1×0.1-mm cross-sectional area. A 90° bend is placed just beyond the end of the reduction transition as shown in Fig. 8. An array of 16×16 of the "multi-fiber" reducers are assembled within a light-tight housing to form the complete image reducer. Using this approach an imager assembly can be made to be 15 cm thick. The composite device consists of 256×256 fibers viewing an area 40×40 cm. The output image area is 3×3 cm. Instead of a lens, the output end of the fiber-optic imager is coupled directly onto a low light-level (Newvicon) video camera equipped with a glass optical fiber faceplate, via one additional array of high-resolution glass-fiber reducers. The video camera has a 1.2×1.2-cm diagonal sensor that views about 36×36 cm of the input image. As with the mirror systems, the camera is interfaced to a microcomputer via a frame grabber for digitizing the output image.

In order for light to be transmitted down a fiber, it must be incident on the face of the fiber at an angle smaller than the acceptance angle. The acceptance angle must be such that rays that enter the fiber strike the walls at an angle smaller than the critical angle θ_c for total internal reflection. The fiber acceptance angle is determined by the indices of refraction of the polystyrene $n_p \approx 1.5$ and acrylic $n_a \approx 1.4$ and the critical angle of reflection within the fiber

$$\cos(\theta_c) = \eta_a / \eta_p, \tag{9}$$

which is about 21°. For a tapered fiber with large input diameter d_1 and small output diameter d_2, a ray having angle θ_1 with respect to the fiber axis at the input will approach the exit face of the fiber at an angle θ_2 with respect to the output axis where

$$d_1 \sin \theta_1 = d_2 \sin \theta_2. \tag{10}$$

Since the maximum output angle is θ_c, Eq. (10) can be used to calculate the maximum acceptance angle θ_a at the input surface

$$\sin(\theta_a) = (d_2/d_1)\sin(\theta_c). \tag{11}$$

The resulting acceptance angle incident on the reduced fiber is on the order of 2°. The cumulative solid angle of all the individual fibers is a measure of the light gathering efficiency of the fiber-optic reducer. This efficiency ϵ_{fiber}, can be expressed as

$$\epsilon_{\text{fiber}} = [(d_2/d_1)(n_p^2 - n_a^2)^{1/2}]^2 \cdot \tau_{\text{fiber}}, \tag{12}$$

where τ_{fiber} is the transmission through a fiber and the coupling loss at the interfaces and the squared quantity is the numerical aperture of each single fiber. The efficiency in light collection also appears to be sensitive to other design details such as the taper length in the reducers and the type of optical glue that is employed between elements which effect insertion losses at each end of the fiber bundle. The efficiency of a fiber coupler is about the same as that of an efficient lens system.

Several characteristics of fiber-optic reducers have been studied. Resistance to radiation damage was investigated by irradiating a single fiber bundle to 10 kGy with a high dose rate animal irradiator. This dose produced less than 5% loss in the light transmission through a fiber bundle.

The line spread function of the system was measured to determine its resolving power. The approach was similar to that used by Munro *et al.*[21] As the resolution was limited by the input fiber area, a 1-mm slit beam, collimated by two highly polished 12-cm tall copper blocks, was used. The blocks were placed directly on the surface of the metal photon-to-electron converter. The slit beam was aligned parallel with one axis of the fiber-optic imager. Slit images were acquired as the slit beam was moved across individual fibers with the aid of a micrometer attachment to determine the line spread function. The results show that the first prototype was capable of resolving 0.3 line-pair per mm at the detector plane.

Although the bundle-to-bundle packing at the input is within a tolerance of 0.05 mm, minor irregularities in the alignment of the fiber bundles at the output, even as small as 0.1 mm, distort the image because of the small-fiber output dimensions. The problem is further compounded by the minor irregularities of the bundle shapes. Distortion of the output image has been corrected with a geometric map that relates the position of each fiber to a corresponding set of pixels on the display. The mapping is achieved by mechanically scanning a single small light source across the input fiber array. Because of variations in screen thickness, video camera phosphor, light transmission in the bundles, and other sources, the output image is inherently nonuniform in light transmission. Therefore, in addition to the geometric mapping correction, portal images are corrected, or normalized, for the nonuniformity by dividing the imaging data with those of a flood field as described in Eq. (8).

In clinical use, images are acquired and digitized at the $1/30$-s video rate. The gain and the background offset setting of the camera are preadjusted so that the normalized image would present the information most relevant for different anatomical regions. An automatic beam-on detection mode initiates data acquisition $1/30$ s after the beam is detected for improving data statistics, the 8-bit data frames are averaged in 16-bits and at frame rate with the on-board utility function of the frame grabber to produce a final image. Typically, 8 to 128 frames are averaged, equivalent to $1/4$ to 4 s of beam exposure for image formation, depending on the application. For example, the shorter time may be used for studying patient motion or for imaging an unblocked, or "open," beam. Open-beam patient images are very useful for superpositioning with small treatment beam images to mimic the double exposure technique of port films. An example image is given in Fig. 9.

C. Liquid ionization chamber systems

A special class of electronic portal imagers is made up of the scanning liquid ionization chambers or SLIC-EPIDs.
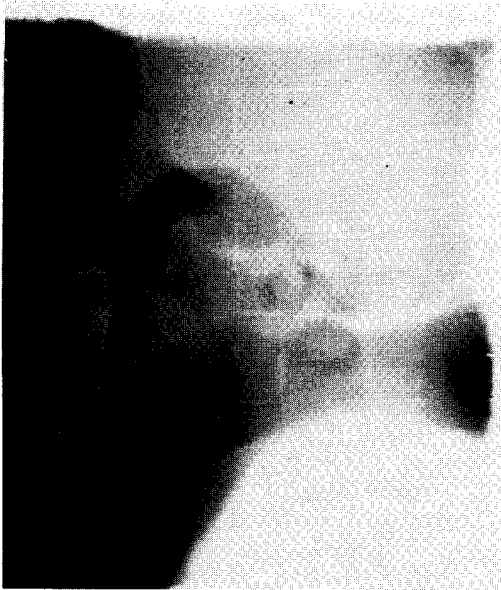
FIG. 9. A 6-MV image produced by a fiber-optic EPID by summing a portal image with a Cerrobend block in place with a full-field image. The portal image was obtained with approximately 5-cGy dose at isocenter and the full-field image was obtained with approximately 2 cGy at isocenter.

Liquid ionization chambers are compact, efficient high-energy x-ray detectors. Ions are created efficiently in a liquid in the volume between high-voltage electrodes. The efficiency of x-ray detection in a liquid is increased over the efficiency of x-ray detection in air in proportion to the density of the liquid relative to the density of air. Organic fluids have been used as the ionized medium in these devices. The two most important factors that influence the choice of the liquid in a SLIC-EPID are (1) charge integration in the liquid and (2) charge collection from the liquid. Both of these processes are influenced by the mobility of the charge carriers. One may place all organic fluid ionization chambers in one of two categories: those relying on ion transport and those relying on electron transport.

1. Matrix ion chamber EPIDs

An imaging system that employs ion transport in a liquid has been developed at The Nederlands Kanker Instituut (NKI). The NKI portal imaging system consists of a 256×256 matrix ionization chamber and a microcomputer system for control and image processing.[37-39] Figure 10 shows a schematic diagram of the imaging system with: (1) the "camera" cassette and (2) the control unit. The camera cassette is quite small having outer dimensions of $525 \times 525 \times 40$ mm and a weight of 7 kg. It contains the following parts: a 256-channel electrometer system, a 256-channel high-voltage switch system, and control electronics. The ionization chamber matrix consists of two double-sided printed circuit boards (standard glass fiber, 0.5-mm-thick front board and 1.5-mm-thick rear board) with etched electrode strips inside the chamber and guarding plates outside the chamber.

A 1-mm liquid film (Iso-octane, spectroscopical pure, Merck) serves as the ionization medium. In addition to the printed circuit boards and the liquid, there is a 1.0-mm-thick stainless steel front screen that acts as the main radiation buildup material. The chamber and metal screen are packed
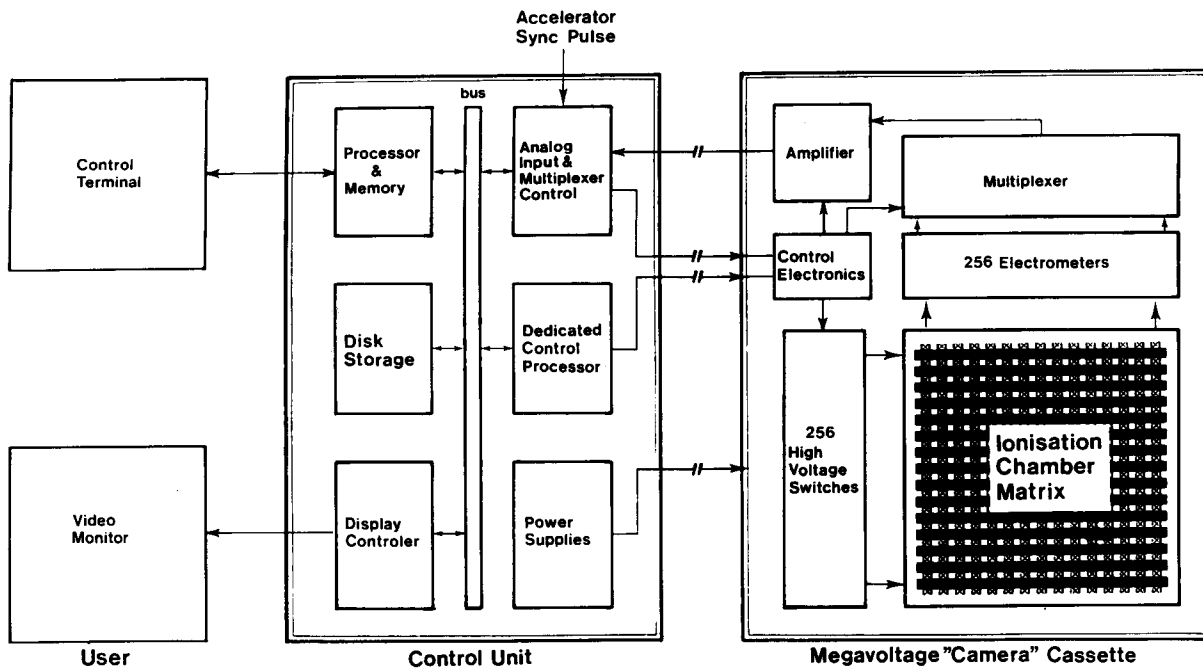

FIG. 10. Schematic of the liquid ionization imaging system. Two sets of perpendicularly oriented electrodes are separated by a 1-mm fluid-filled gap. The strip electrodes are effectively scanned by sequentially activating the perpendicular high-voltage electrodes.

between two carbon fiber reinforced foam boards of low density that form part of the cassette housing. There are 256 strip-formed electrodes on the rear plate that serve as signal electrodes. Each strip is connected to a sensitive electrometer. At right angles to the signal electrodes on the opposite plate are 256 high-voltage electrodes. Each high-voltage strip is connected to a high-voltage switch. The signal and high-voltage electrodes cross each other perpendicularly. Each crosspoint acts as a small ionization chamber. The resolution of the system is determined by the 1.27-mm spacing of the electrode strips. The entire matrix thus consists of 256×256 ionization chambers giving a total field of view of 325×325 mm. To obtain one image, the ionization matrix is scanned row by row, by successively switching high voltage to different voltage electrodes and measuring the currents in all 256 column electrodes. The ionization chambers operate at a polarizing voltage of 300 V, which is well below saturation for the liquid. This voltage is limited by technical constraints of the switching circuits. A typical current produced by each ionization chamber in an 8-MV x-ray beam is 50 pA when exposed to an air kerma rate of 200 cGy/min. The outputs of the 256 electrometers are multiplexed to a single amplifier and digitized in the control unit. The electrometers can measure signals up to 4 nA with a noise level of about 0.5 pA. To improve the SNR, sequential electrometer output values are averaged digitally. Each electrometer contains a presampling filter with a time constant adapted to the measuring speed.

The 256 high-voltage electrodes are controlled by a circuit that switches each high-voltage electrode separately. The setting of all the high-voltage switches can be changed once each 1.3 ms, which is the time needed for the serial transfer of the switch-setting data. The camera cassette furthermore contains electronics for the following functions: (1) time demultiplexing of control signals which allows the unit to be controlled by only two lines, (2) power supply stabilizers for minimal supply noise, and (3) the signal amplifier for the multiplexer output.

The cassette subsystem is operated by a data acquisition and control subsystem. The control unit consists of a 16-bit microprocessor (80286, Intel) with 2 Mb of RAM, and disk storage. The microprocessor programs control the image acquisition. A 200-kHz 12-bit A/D converter uses an input amplifier with software-selectable gain. A control circuit time multiplexes the control lines and a display processor provides a 512×512 pixel, 8-bit grey scale image. The microprocessor can sample an external synchronization line, which can be connected to the accelerator "scope trigger" signal. All imaging parameters such as scanning speed, high voltage, etc. can be changed with simple commands to optimize system performance. A standard image is made and displayed in 5.9 s. In this time the current of each ionization chamber is measured ten times, and the values can be averaged. To reduce the time required for switching the high-voltage electrodes, the image matrix is scanned only once, so that the measurement cycle is 256 times "switch to next high-voltage electrode," and 6 times "measure 256 signal electrodes." As the ionization chamber readout is rather fast (20 ms for one row of 256 ionization chambers averaged six

times), all operations can be synchronized to the accelerator pulse frequency (typical 200–400 Hz), to avoid interference between accelerator pulses and image scanning. Recent results show that due to the long ion lifetime in the liquid, the unsynchronized read-out can be used with hardly any loss in image quality. As a result of the high-voltage switching, a transient pulse is induced in the electrometer amplifiers. After this it takes about 5 ms before the electrometers can be used again. This time is used for corrections and display.

In the same 5.9 s, the electrometer offsets have been determined accurately. This is necessary because the electrometer offsets are influenced by stray radiation and temperature. This measurement also corrects for the signal that is produced by the ionization chambers without polarizing voltage. In addition to the slow normal scanning mode described above, the following modes have been developed.

(1) Slow smooth mode: Three neighboring voltage electrodes are at high voltage at the same time. This triplet traverses the matrix in steps of one voltage electrode, with 20 ms between the consecutive 256 steps. The image is acquired in 5.9 s. Averaging over three electrodes has the effect of reducing the noise at the expense of a lower spatial resolution in one direction. An example of the application of this mode would be the imaging of pelvic fields where contrast resolution is of major importance.

(2) Fast smooth mode: Like the slow smooth mode, but with 10 ms between switching high voltages instead of 20 ms. The image is acquired in 2.9 s. The noise level is slightly higher.

(3) Ultra half mode: Two neighboring voltage electrodes are at high voltage at the same time. This doublet traverses the matrix in steps of two voltage electrodes with 10 ms between the consecutive 128 steps. The image is acquired in 1.5 s. The spatial resolution is reduced in one direction. This mode is typically needed for the double exposure technique. Important specifications like the scan time, spatial resolution and noise are given in Table I for these clinically relevant acquisition modes.

The image is constructed within the microprocessor from the digitized ionization currents. The following corrections are performed on the raw image data: (1) Electrometer offset and/or leakage corrections are always performed during the imaging process. The magnitude of this correction is about 10%. The correction values are measured automati-

TABLE I. Scan time, spatial resolution, and noise for four acquisition modes with the liquid ionization EPID. The spatial resolution is given by the full width half-maximum (FWHM) of the line spread function (LSF). Note that the FWHM varies only in one direction for the various modes.

Mode name	Scan time (s)	Spatial resolution (mm)	Noise level %
Slow normal	5.9	2.3×2.9	0.28
Slow smooth	5.9	2.3×4.3	0.13
Fast smooth	2.9	2.3×4.5	0.19
Ultra half	1.5	2.3×3.1	0.25

cally by the imaging software. (2) During calibration, which is typically performed once a week to once a month, individual ionization chamber offset values are measured, by acquiring an image without radiation. The application of this correction copes with artifacts caused by the fast switching of the high-voltage electrodes. Leakage currents in the liquid were negligible. The magnitude of this correction is about 1%. (3) At the same calibration session, the sensitivity of each ionization chamber is determined by acquiring a flood field image. Calibration data is stored separately for all three acquisition modes. The total magnitude of this correction can be up to 40%. Sources of sensitivity variations among individual ionization chamber cells are electrode shape differences and of electrode surface inhomogeneities. The ionization chamber sensitivities also depend on the local thickness of the liquid layer. Corrections (2) and (3) are described in Eq. (8).

The image correction and display operations are performed during the imaging process itself. In this way an image is built up on the screen at the same time that the ionization chambers are scanned. The reconstruction and display operations are then performed in the time just after the switching of the high-voltage electrodes, which otherwise would have been spent waiting. An example of an image produced by the liquid ionization EPID is given in Fig. 11.

2. Electron transport SLIC-EPIDs

An important feature of the organic liquids suitable for use in room-temperature liquid ionization chambers is that the mobility of the molecular ions is up to $\sim 10^5$ times less than that of the excess electrons[40-44] and is of the order of 5×10^{-4} cm^2 V^{-1} s^{-1}. However, in all known room-temperature liquids suitable for use, the ionization electrons are trapped in nanoseconds or less forming slow-moving ions. This is due to the presence of electronegative impurities in the liquid.[40,41,44] In order to measure the ionization electrons created in room-temperature fluids, the electron-trapping impurities (Cl,O,OH,H_2O,etc.) must be reduced to levels of

FIG. 11. An image produced by the liquid ionization imaging system. The image shows a thoracic vertebra imaged by 8-MV x rays by averaging four images during a dose of 100 cGy at isocenter.

parts-per-billion.[41] Failing to do so means that the signals measured from chambers using such fluids are derived entirely from the drift of ions in the electric field. A potential improvement in the performance of SLIC-EPIDs may be achievable through the use of part-per-billion clean liquid dielectric for the ionization medium. While the NKI imager is a successful example of the use of an ion transport liquid, the development of an "electron transport" imager would result in a device with completely different parameters which might offer significant potential advantages.

The advantage of relying on ion transport (low mobility) is that the ion lifetime is very long, resulting in an inherent charge integration in the liquid. The inherent "effective integration time" for an ion transport chamber has been shown to be inversely proportional to the square root of the ionization rate times the ion mobility.[42,43] Under "normal" radiotherapy conditions the ion lifetime in the NKI imager is reported to be about 0.5 s. This means that, even though an image is scanned in about 5 s by switching the voltage between rows of electrodes over the whole chamber, the information that is obtained is due to 0.5 s of exposure. This corresponds to a "sampling efficiency" of about 10%. This is much better than the sampling efficiency of a nonintegrating system which, for 256 rows, would have an efficiency of 1/256 or 0.4%. While such integration is not feasible for an "electron-transport" SLIC imager since the maximum electron lifetimes are currently only approaching the millisecond range, the far higher mobility of electrons offers a direct method of greatly increasing the charge collection efficiency resulting in a decrease in the irradiation time needed to form an image. To quantify this advantage imagine two chambers of identical design—one of which uses electron transport, the other of which uses ion transport. For concreteness, let the geometry of the chambers be essentially that of the existing NKI chamber with a 1-mm gap between the two planes of electrodes.

The radiation from a therapy machine is typically delivered in 2 to 5 μs bursts every 12.5 to 5 ms. In the NKI imager, 300 V applied across the 1-mm gap gives rise to an ion drift velocity of 2.4 mm s^{-1}, using the published mobility[42,43] of 8×10^{-5} cm^2 V^{-1} s^{-1}. Thus the time for an ion to drift across the 1-mm gap would be ~ 400 ms. During actual operation, the voltage is applied for only ~ 20 ms, and thus the fraction of available ion charge that is collected is about 5%. This poses a limitation on the read-out speed of the NKI imager. A lower collection fraction, for example when sampling an electrode for only 10 ms, would increase the relative noise contributions of the amplifiers. In comparison, the very high mobilities offered by an electron transport imager would result in much faster and more complete signal collection at lower voltages. For example, a 50-V bias across a 1-mm gap allows electrons to traverse a fluid in the gap in less than 7 μs. Under such conditions, virtually all of the available electron signal could be extracted for a large fraction, and possibly all, of the imager's chambers between successive bursts of radiation. Following each burst of radiation, voltage would be applied to successive voltage electrodes, one electrode at a time. Seven microseconds would be sufficient to allow simultaneous collection of $\sim 100\%$ of the
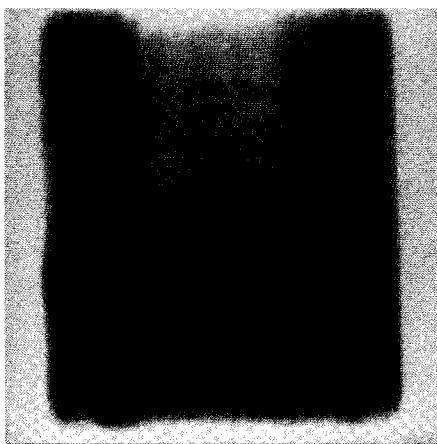
charge from the signal electrons in all chambers along a selected row using parallel amplifiers. This process would be repeated row-by-row until the entire imager is read out or until the electrons have decayed away. The sequence would be continued following each radiation burst averaging the signals until an acceptable image is formed.

The advantages of this approach are that (i) any desired amount up to $\sim 100\%$ of the electron signal may be sampled per electrode and (ii) a very large fraction of the chamber could be scanned burst-by-burst. For instance, with a burst repetition rate of 200 Hz (1 burst every 4 ms) there would be sufficient time to read out each 256-electrode chamber within the ~ 1.8 ms (256 rows $\times 7 \mu s$) needed for actual signal collection. As the number of high-energy quanta sampled would be only those from the preceding burst, the entire chamber would have to be repeatedly sampled over a sufficiently large number of bursts and the data summed in order to acquired a suitable image. Consequently, providing that the electron lifetime is of the order of 2 ms, an electron transport imager should be capable of producing images of comparable quality to that of an ion transport imager in an irradiation time comparable to the reported ion-integration time of the NKI imager (~ 0.5 s).

Recent progress in the development of detectors for particle physics applications support the feasibility of attaining suitable long electron lifetimes for an electron transport SLIC imager. Following the discovery[45] of highly mobile electrons in ultrapure hydrocarbons in 1977, a number of groups have been pursuing the development of ionization chambers using tetramethylsilane[46] (TMS) [$(CH_3)_4Si$], and tetramethylpentane[44] (TMP) (C_9H_{20}). A particle physics collaboration at CERN has constructed 20 000 TMP-filled detectors[44,47] and fluid cleaning procedures have been refined to the extent that electron lifetimes of 300 to 400 μs have now been achieved. Furthermore, free electron lifetimes of 77 and 450 μs with TMP and TMS, respectively, have been independently reported.[48] An important unresolved question concerning the possibility of maintaining such long lifetimes in a radiotherapy imager revolves around the concern that, due to the high dose rate and scanning operation of an SLIC imager, the free electron lifetime could be severely limited by recombination.

The disadvantages of the electron transport approach are as follows. First, as integration of information is no longer taking place in the chamber, it is necessary to process the analog and digital information for all, or a fraction of, the entire chamber on a burst-by-burst basis and integrate this information digitally in a buffer. This is not as convenient as allowing the chamber to integrate the information itself, and would require handling data rates of ~ 13 MHz in the case of a 256×256 element imager operated at 200 pulses-per-second. However, such data rates can be accommodated using existing analog and digital signal processing hardware and techniques. Second, the fast ($\sim 1 \mu s$) switching of even modest voltages (~ 50 V) will introduce transients whose signal size will be comparable to the measured signals. However, various schemes may be possible to effectively deal with this problem involving changes to the electrode structure of the chamber and/or signal processing techniques. The feasibil-

ity of developing an electron transport imager is currently under examination by a group at the Department of Radiation Oncology at the University of Michigan.

3. CT reconstruction liquid ion chamber EPID

An alternate way of using liquid filled ionization chambers for portal imaging is being pursued by Bova.[49,50] This system would consist of 256 long, thin ionization chambers, each of dimension $2 \times 2 \times 220$ mm. The chambers would be positioned so as to form a detection plane. In each chamber a 2-mm gap filled with liquid ionization medium is bounded by a pair of long parallel electrodes. A constant high voltage (2 kV) is applied to the voltage electrode, and a signal is extracted from the collecting electrode. A guard electrode in the design helps shape the applied electric field. Thus each chamber would sample the radiation along a narrow (~ 2 mm) strip. During operation, the entire plane of chambers rotates about an axis perpendicular to the plane of the detectors, and spatial information is encoded by registering the collected currents from all 256 chambers as a function of angular position. The image is then reconstructed by means of a filtered back-projection technique.

Using a single prototype chamber, Bova has demonstrated the feasibility of this concept by suitable rotation and translation of the chamber. A spatial resolution of 4.12 mm in the reconstructed image was achieved requiring 0.025 cGy per angular sample to form the image. A total of 180 angular samples were required per image and the total beam accumulation time was 4.5 s.

The thin-box construction and wider gap allow these chambers to operate at a significantly higher voltage than the NKI imager. Also, as there is no need to switch the voltage on and off in this scheme, the proposed system would not need to contend with the switching transients suffered by both the NKI and proposed electron transport imager. This ought to greatly simplify the electronics for the rotating system. However, long-lived ions in the medium could limit the speed at which this system could be rotated.

D. Solid-state systems

A nonoptical approach involving a scanning linear array of silicon diodes has been pursued by a group at Johns Hopkins.[51-53] This approach employed high-voltage rectifier diodes.[54,55] As depicted in Fig. 12, a linear array of 255 diodes is arranged with a center-to-center spacing of 2 mm between the diodes. A 1.1-mm-thick Pb strip covers the diode array, and the array is placed 150 cm from the source. During image acquisition, the linear array is scanned, in 2-mm increments, across the field of interest by means of a stepping motor operated by computer. For each radiation burst, signals from all 255 diodes are amplified, multiplexed, and digitized to 12-bits. Data are acquired at each stepping position for a significant number of bursts in order to create a single line in the image.

For a 4-MV beam the group reports being able to resolve objects of 0.8% primary subject contrast using a dose of 0.27 cGy for each line of the image. As this system only utilizes a small fraction of the radiation field, large doses are required
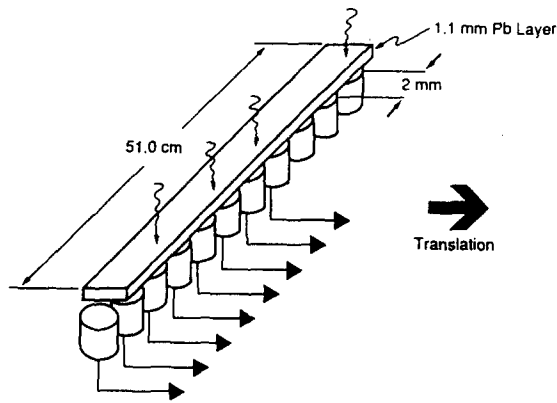
FIG. 12. A diode array EPID consisting of a linear array of discrete radiation diodes that are mechanically translated across the x-ray beam to form the image. The diodes are spaced 2 mm apart. The lead layer acts as the x-ray detector.

to form an image with this contrast. For example, imaging a 20- to 45-cm-long radiation field requires a total dose of 27 to 60 cGy. A second limitation is the comparatively large interdiode spacing, leading invariably to coarser spatial resolution than is possible with finer detail systems such as the fluoroscopy camera devices. Finally, prospects of creating a two-dimensional array of such diodes are dim given the enormous complexity and expense which the assembly and wiring of such a scheme would entail.

Another approach involving the scanning of a linear array of detectors across the field has been pursued by Morton and Swindell at the Royal Marsden Hospital.[56] The arrangement is shown in Fig. 13. The array consists of a double row of zinc tungstate ($ZnWO_4$) scintillating crystals. Each crystal is $5 \times 5 \times 25$ mm. The crystals are arranged in a double row, 64 crystals per row, with the rows offset by half a crystal width, and, during image acquisition, the array is scanned in steps of half a crystal width. This geometry and scanning protocol exactly satisfies the Nyquist sampling interval for this detector. While both $ZnWO_4$ and bismuth germanate (BGO) were considered, the former was chosen because of measurements that indicated superior (2.3x) light output for this particular detector geometry and electronics. In order to maximize the detected light signal, the faces of each crystal were carefully polished and coated with a diffuse reflective material with the exception of a single output face to which a photodiode was optically coupled. Diode noise was minimized by operating the diodes at zero bias. The diodes were operated at zero bias is order to (1) eliminate leakage current and its associated noise; (2) allow temporal integration in the electronics with no build-up of dark signal which would otherwise dominate the x-ray induced signal; and (3) assure linear diode response with signal intensity.

During image acquisition high-energy photons that interact and create high-energy electrons that pass through the volume of these crystals result in the creation of a visible light signal that is detected by the photodiodes. As the crystal is optically transparent a relatively long detector is possible (25 mm) and this results in a very high efficiency for the
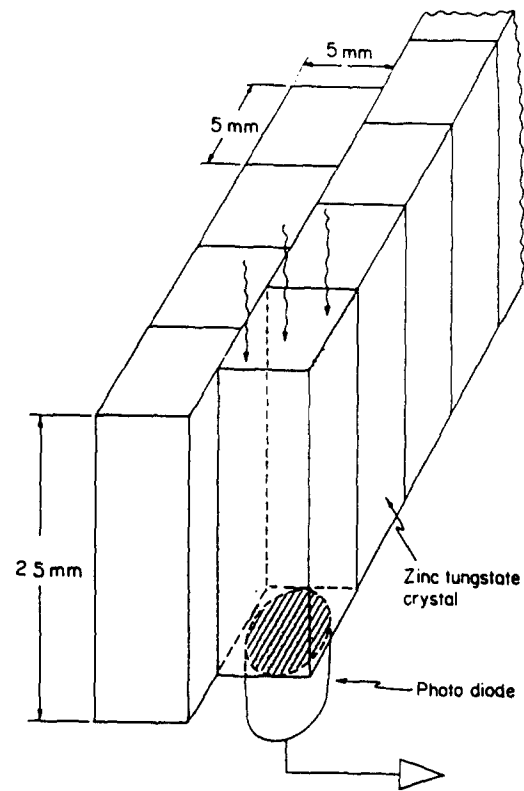

FIG. 13. A solid state EPID consisting of a linear array of discrete $ZnWO_4$ crystals. The x-ray induced scintillation of each crystal is detected by a photo diode. To increase the linear resolution, every other crystal/diode detector is offset one half crystal width.

detection of the high-energy photon quanta (~50% at 6 MV). At each stepping position, signals from the diodes are processed using analog filtering so as to allow signal integration over ~0.1 s. The integrated signals are multiplexed and digitized to 12 bits.

The high quantum-efficiency of the system allows images to be produced with ~20 cGy for a 17×17-cm radiation field with objects of 0.5% primary subject contrast detectable. This group has employed the same general detection principle to create a computed tomography (CT) scanner for radiotherapy beams.

The many constraints and demands posed by real-time megavoltage radiotherapy imaging make a large-surface-area, radiation-resistant, solid-state imager a very attractive goal for this application.[57] Recent developments in the materials science and technology of hydrogenated amorphous silicon made such an imager feasible.[58-60] Hydrogenated amorphous silicon (a-Si:H) is a relatively new silicon alloy exhibiting some of the desirable properties of crystalline solid-state materials. Various a-Si:H devices such as diodes and thin-film transistors are routinely fabricated on a substrate (such as glass or quartz) by gas deposition in a reaction vessel.

Since the preparation method is from gases, arrays of a-Si:H devices can be very large compared with crystalline silicon wafers. For example, solar cell arrays are commonly fabricated on 50×50-cm substrates or on continuous rolls of

stainless steel. In particular, large arrays of a-Si:H transistors are under intense development in conjunction with the flat-panel display industry and 14-in. diagonal displays containing ~ 1.5 million field effect transistors (FETs) have already been demonstrated.[61] The imager's sensors are photodiodes consisting of a bottom metal contact, an n-doped layer, an intrinsic i-layer, and a p-doped layer, with a final transparent metal contact on top. A reverse bias is applied to this diode in order to fully deplete the i-layer. These photodiodes would be arranged in a regular Cartesian grid in a two-dimensional array as shown in Fig. 14. Attached to each photodiode is a single thin-film FET. All gates for the FETs for a given row of photodiodes are connected to a common FET line. The source of each FET is connected to its associated photodiode, and all the drains for the FETs in a single column are attached to a common DATA line.

This a-Si:H array would be positioned immediately below a metal plate and phosphor screen combination; both the plate and the screen have functions identical to those in the fluoroscopy camera systems. In fact, the a-Si:H array serves as a direct substitute for the mirror, the light box, and the camera or for the fiber-optic lines and the camera in the other "optical" systems. During image acquisition, all the FET lines are kept at a negative voltage so as to make the entire array of FETs nonconducting. Light emitted by the phosphor is converted with high efficiency into electron-hole pairs in the i-layer of the photodiodes and collected and stored in the capacitance of the photodiodes. When sufficient signal has been collected for an image, the stored signals are read out, one row at a time. This is accomplished by changing the voltage on the corresponding FET line so as to make all the FETs along that line conducting. This allows

the signals stored in the photodiodes to propagate through the FETs onto the DATA lines. These signals are then processed and digitized by external electronics. The voltage on the FET line is returned to its initial state and the process is repeated for the next row until the entire array has been read out. This may be repeated each time a new image frame is desired.

Compared with the other optical systems, an advantage of using an array of photodiodes placed in close proximity to the phosphor is that a very high percentage of the emitted light may be intercepted and converted to signal. While this percentage easily exceeds 50% in the a-Si:H imager configuration, it is considerably less than 1% in the fluoroscopy camera and fiber-optic systems. In addition, such an a-Si:H would be very compact, with a total thickness about that of a film cassette.

While such a photodiode array could conceivably be constructed from crystalline silicon materials, several factors make a-Si:H a superior choice. First, the very nature of the technology lends itself to large surface areas devices. As crystalline silicon devices are ultimately limited by the size of commercially available wafers, large arrays of such devices for medical imaging would have to be made up of many smaller tiles. This would be a very difficult and demanding engineering task. Second, as the commercial interest in flat panel displays is spurring the development of larger and larger arrays, the heavy investments in research and development and production facilities will be born by the display industry and not by the considerably smaller medical imaging industry. Finally, amorphous materials are particularly well suited to megavoltage imaging because of their inherent radiation resistance.[59,62]
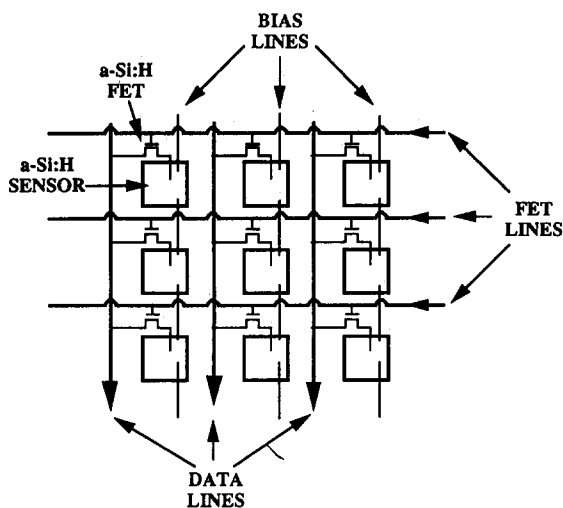

FIG. 14. Top schematic view of a section of an amorphous silicon imaging array consisting of photodiode sensors and field effect transistors (FETs). Sensors in each column are connected to a common DATA line by the FETs. The gates for each row of FETs are connected to a common FET control line. During imaging, FETs are kept nonconducting to allow charge to accumulate in the sensors. To sample this charge, the FETs are rendered conducting, one row at a time, allowing the sensors' charge to propagate onto the DATA lines and thereafter to external readout electronics.

IV. APPLICATIONS

The definitions of localization and verification portal images in this paper are in line with the definitions recommended by the AAPM.[63] A portal image for purpose of localization is produced by an exposure that is short compared with the treatment time. These portal images can be used in an interactive manner to adjust the patient setup and field boundaries prior to the administration of the major portion, for instance 80% to 90%, of the daily dose. For a typical single-field dose of ~ 100 cGy at dose maximum, a portal image should be acquired during the delivery of less than 1 to 20 cGy, which corresponds to an acquisition time of about 0.25 to 5 s for a dose rate of 2.5 Gy min^{-1}.

For evaluation of a setup where a high accuracy is required, usually *a priori* knowledge is available about the position of the field edges relative to anatomical structures. The intended setup is documented either (1) on a simulator image obtained for an identical set up at the simulator or (2) on a digitally reconstructed radiograph (DRR), which has been reconstructed for a chosen treatment beam setup from a series of CT images.[64,65] In case no reference image is available, the adequacy of the setup must be determined from an initial portal image.

In addition to the necessity of a fast on-line EPID, it is

obvious that for clinical application of portal localization images this device must be provided with a number of fast image processing utilities. These utilities are crucial for a quick setup evaluation, i.e., an evaluation within 1 to 2 min. The following utility functions are needed: (1) display of the portal image, (2) display of a reference image, (3) field edge position quantification, (4) autolevel and window setting, (5) image enhancement, and (6) automatic or semiautomatic setup evaluation. An image displayed near the therapy machine operator's console within a few seconds of the x-ray exposure is also mandatory for routine clinical practice. In this time period some image processing must be performed before the portal images can be analyzed by the physician or the technologist.

For a completely automatic evaluation, even faster algorithms are needed that can evaluate a patient setup within a few seconds after the acquisition of the portal image. The results of this evaluation could then be used to interrupt the irradiation automatically in case tolerance levels are exceeded.

The reference image, corresponding to the intended treatment field, should be displayed prior to starting the irradiation. If simulator film images are used, they must have been previously digitized for that purpose. In case DRRs are utilized, it must be possible to transfer these digital images, which are usually generated by a treatment planning system (TPS), from the TPS to the EPID. Because the simulator images and DRRs are available quite some time before the irradiation starts, time constraints are not present for preprocessing of these reference images. Utilities should be provided to mark relevant information for the evaluation in these images, such as the position of the central axis, the major axes, the field edges and anatomical structures.

The position of the field edge is of great importance for evaluating the setup. Further image processing, such as that done to improve image quality, may cause this position to deteriorate. It is therefore necessary to start with the detection of the field edge first, preferentially in an automatic way.[66] Once the coordinates of the edge pixels are stored, these pixels can be highlighted in enhanced images and further be used for image analysis.

A number of digital methods have been investigated for improving the discernability of anatomical landmarks in portal images. Various histogram modification techniques are quite efficient for contrast enhancement.[11,67–70] The same number of image pixels are assigned to each display level, i.e., the display level histogram is equalized. It has also been demonstrated that, for contrast enhancement and improved sharpness, an inverse frequency filter technique, combined with a low-frequency cutoff filter, significantly improve the image quality.[71] The inverse filter corrects for the blurring phenomena of the complete imaging chain, including the focal spot size, while the cutoff filter eliminates gross variation in pixel value over the portal image, which is due to gross variations in intensity over the radiation beam. This filter method resembles the unsharp masking technique.[72] In addition, simple convolution filters such as Laplacian and smoothing filters and combinations of these filters can be applied successfully.[64]

The distribution of the values of pixels that are inside the image of the port depends on many factors like beam intensity, use of a wedge filter, patient thickness, patient outline, patient-to-detector-distance, and detector parameter settings. This distribution is important for a proper level and window setting for image display and can only be determined after acquisition of the image data. Prior to the irradiation, estimated level and window values can be set. Once the data acquisition has been completed, proper settings can be determined, for instance, from data already available for auto edge detection or image enhancement.[66]

The goal of the field verification is to evaluate the locus of the field edge contour relative to the observable patient anatomy. The task can be considered to be the determination of two types of positions: (1) the position of the field edge contour with respect to the axis of rotation of the accelerator collimator, and (2) the position of identifiable anatomical contours with respect to the axis of rotation of the accelerator collimator. Three different approaches for setup analysis can be considered which depend on the EPID operating conditions: (1) The EPID is rigidly mounted (with less than 0.5 pixel position shift for all gantry angles), (2) a reference graticule, mounted at the head of the accelerator, is imaged simultaneously, or (3) the only *a priori* information is that the imaging plane of the EPID is perpendicular to the central axis of the beam.

A rigid mounting arrangement provides the most opportunity for field verification. The reference image matrix can easily be matched to the portal image matrix by aligning the major field axes and by correcting for the differences in magnification. The actual outline of the radiation field and the intended outline can be directly compared visually or by application of distance and angle measuring features. However, a high positional accuracy of the EPID for all gantry angles relative to the accelerator is a challenging engineering problem. The EPID and its mounting structure should interfere as little as possible with the patient setup activities of the technicians. In particular, the arrangement should not interfere with the use of a laser alignment system. For a quantitative analysis of the position of anatomical structures inside the beam, these structures may still have to be delineated first in the portal image.[73]

A graticule mounted near the head of the irradiation machine can project mutually perpendicular arrays of equi-spaced dots on the EPID, similar to those projected by a graticule on a simulator.[74] The transfer of the reference image to the portal image can be found by matching the graticule points in both images. A number of difficulties must be overcome in order to use a graticule. Unless special software automatically identifies the graticule points, they must be identified manually. In addition, the graticule must be removed from the beam before the rest of the dose is administered. The removal requires a technician to reenter the treatment room adding time and effort back to the localization process.

On the other hand, if the EPID is less rigidly mounted on the linear accelerator [option (3) above], the imaging plane of the EPID may still be considered to be perpendicular to the central axis of the beam. In addition the focus-to-detec-

tor distance might be known. However, no further information on the position of the EPID would be available. Matching of the portal image to the reference image must be done by either: (a) matching of field edges (b) matching of anatomical structures.[73]

Matching of anatomical structures can be time consuming when a large number of these structures have to be delineated manually in the portal image matrix after this image has been displayed.[74] In addition, this delineation has to be done accurately in order to obtain a match with sufficient accuracy.[75] To facilitate this procedure, corresponding relevant structures that have already been delineated in the reference image can be applied. In this way the procedure may be reduced to the adjustment (magnification, rotation, and translation in two directions) of stored structures, which might be less time consuming. After this interactive delineation procedure, the information of the position of the various structures in the reference and in the portal image can be used for a fast match of both field images. However, with all manual procedures, a subjective element is introduced into the evaluation.

To fully integrate an EPID in routine clinical practice, in particular for fast evaluation purposes, new methods for automatic setup evaluation are mandatory. It is essential that techniques for automatic extraction of anatomical structures from portal images, which are inherently of poor quality, will become available. Various image filtering procedures (e.g., edge enhancement filters and morphologic filters) might be useful for this purpose. These techniques still have to be developed and evaluated.

A more sophisticated method for field placement analysis should also take into account the three-dimensional aspect of the setup. Matching of anatomical structures in the corresponding reference image and portal image of a single field is sometimes inaccurate.

This occurs because only rotation around the central axis and two orthogonal translations perpendicular to the central axis are usually taken into account. In fact, six degrees of freedom are involved: three rotations around the central axis and around the two orthogonal axes perpendicular to this central axis, and three translations along these three orthogonal axes. For multiple field setups the results for the various fields should be combined because they are correlated. For instance, a misalignment in the longitudinal direction of a patient will be observed in the anterior–posterior as well as in both lateral portal images of a three-field pelvic irradiation. It is then assumed, however, that the patient does not move between the setup of consecutive fields and the administration of the dose.[76]

V. SUMMARY

Electronic portal imaging, although still in its infancy, is well under development. Commercial devices are available for purchase that can be used clinically. These devices already provide images that are comparable to radiographic film but have the advantage that the images are viewable within seconds of the exposure and are stored and transferred electronically. Concepts of the physics of fluence con-

version, image formation, optics, and principles of data manipulation have been borrowed from other fields. This body of knowledge has been extended and integrated to form the fundamentals upon which EPIDs have been constructed. This review has demonstrated the potential for development of advanced imaging devices, image enhancement and evaluation software, and clinical applications for EPID technology.

ACKNOWLEDGMENTS

[1] J. E. Marks, A. G. Haus, G. H. Sutton, and H. L. Griem, "Localization error in the radiotherapy of Hodgkin's disease and malignant lymphoma with extended mantle fields," Cancer **34**, 83–90 (1974).

[2] L. V. Verhey, M. Goitein, P. McNulty, J. E. Munzenrider, and H. D. Suit, "Precise positioning of patients for radiation therapy," Int. J. Radiat. Oncol. Biol. Phys. **8**, 289–294 (1982).

[3] I. Rabinowitz, J. Broomberg, M. Goitein, K. McCarthy, and J. Leong, "Accuracy of radiation field alignment in clinical practice," Int. J. Radiat. Oncol. Biol. Phys. **11**, 1957–1867 (1985).

[4] H. Huizenga, P. C. Levendag, P.M.Z.R. De Porre, and A. G. Visser, "Accuracy in radiation field alignment in head and neck cancer," Radiother. Oncol. **11**, 181–187 (1988).

[5] R. W. Byhardt, J. D. Cox, A. Hornburg, and G. Liermann, "Weekly localization films and detection of field placement errors," Int. J. Radiat. Oncol. Biol. Phys. **4**, 881–887 (1978).

[6] G. K. Svensson. "Quality assurance in radiation therapy: Physics efforts," Int. J. Radiat. Oncol. Biol. Phys. Sup. 1 **10**, 23–29 (1984).

[7] M. Goitein and J. Busse, "Immobilization error: some theoretical considerations," Radiology **117**, 407–412 (1975).

[8] J. E. Marks, A. G. Haus, H. G. Sutton, and M. L. Griem. "The value of frequent treatment verification films in reducing localization error in the irradiation of complex fields," Cancer **37**, 2755–2761 (1976).

[9] H. I. Amols, L. E. Reinstein, and B. Lagueux, "A quantitative assessment of portal film contrast as a function of beam energy," Med. Phys. **13**, 711–716 (1986).

[10] H. Meertens. "Digital processing of high-energy photon beam images," Med. Phys. **12**, 111–113 (1985).

[11] J. Leong, "A digital image processing system for high energy x-ray portal images," Phys. Med. Biol. **20**, 1527–1535 (1984).

[12] N. A. Baily, R. A. Horn, and T. D. Kampp, "Fluoroscopic visualization of megavoltage therapeutic X-ray beams," Int. J. Radiat. Oncol. Biol. Phys. **6**, 935–939 (1980).

[13] H. Meertens, M. van Herk, and J. Weeda, "A liquid ionization detector for digital radiography of therapeutic megavoltage photon beams," Phys. Med. Biol. **30**, 313–321 (1984).

[14] J. W. Motz and M. Danos, "Image information content and patient exposure," Med. Phys. **5**, 8–22 (1978).

[15] H. E. Johns and J. Cunningham, *The Physics of Radiology* (Charles C. Thomas, Springfield, IL, 1983), 4th ed.

[16] J. E. Motz and C. E. Dick, "X-ray scatter background signals in transmission radiography," Med. Phys. **2**, 259–267 (1975).

[17] D. W. O. Rogers, "Fluence-to-dose equivalent conversion factors calculated with EGS3 for electrons from 100 KeV to 20 GeV and photons from 11 keV to 20 GeV," Health Phys. **46**, 891–914 (1984).

[18] K. Doi, G. Holje, L-N Loo, H-P Chan, J. M. Sandrik, R. J. Jennings, and R. F. Wagner, "MTF's and Wiener spectra of radiographic screen-film systems," HHS Publ. No. 82-8187 (FDA) (1982).

[19] R. T. Droege, "A megavoltage MTF measurement technique for metal screen-film detectors," Med. Phys. **6**, 272–279 (1979).

[20] P. Munro, J. A. Rawlinson, and A. Fenster, "Therapy imaging: A signal-to-noise analysis of metal plate/film detectors," Med. Phys. **14**, 975–984 (1987).

[21] P. Munro, J. A. Rawlinson, and A. Fenster. "Therapy imaging: a signal-to-noise analysis of fluoroscopic imaging system for radiotherapy localization," Med. Phys. **17**, 763–772 (1990).

[22] P. Munro, J. A. Rawlinson, and A. Fenster, "Therapy imaging: limita-

tions of imaging with high-energy x-ray beams," Proc. S.P.I.E. Med. Imag. **767**, 178–184 (1987).

[23] J. C. Dainty and R. Shaw, *Image Science* (Academic, New York, 1974), Chaps. 6 and 8.

[24] R. M. Nishikawa and M. J. Yaffe, "Signal-to-noise properties of mammographic film-screen systems," Med. Phys. **12**, 32–39 (1985).

[25] W. R. Lutz and B. E. Bjarngard, "A test object for evaluation of portal films," Int. J. Rad. Oncol. Biol. Phys. **11**, 631–634 (1985).

[26] P. Munro, J. A. Rawlinson, and A. Fenster, "A digital fluoroscopic imaging device for radiotherapy localization," Int. J. Radiat. Oncol. Biol. Phys. **18**, 641–649 (1990).

[27] M. Strandquist and B. Rosengren, "Television-controlled pendulum therapy," Brit. J. Radiol. **31**, 576–577 (1958).

[28] H. Wallman and N. Stalberg, "A television-roentgen system for pendulum therapy." Brit. J. Radiol. **31**, 576–577 (1958).

[29] J. R. Andrews, R. W. Swain, and P. Rubin, "Continuous visual monitoring of 2 MeV roentgen therapy," Am. J. Roent. **79**, 74–78 (1958).

[30] S. Brenner, B. Rosengren, H. Wallman, and O. Netteland, "Television monitoring of a 30 MV x-ray beam," Phys. Med. Biol. **7**, 29–34 (1962).

[31] J. Leong, "Use of digital fluoroscopy as an on-line verification device in radiation therapy," Phys. Med. Biol. **31**, 985–992 (1986).

[32] S. Shalev, T. Lee, K. Leszczynski, S. Cosby, and T. Chu, "Video techniques for on-line portal imaging," Comp. Med. Imag. Graph. **13**, 217–226 (1989).

[33] A. G. Visser, H. Huizenga, V.G.M. Althof, and B. N. Swanenburg, "Performance of a prototype fluoroscopic radiotherapy imaging system," Int. J. Radiat. Oncol. Biol. Phys. **18**, 43–50 (1990).

[34] P. Munro, J. A. Rawlinson, and A. Fenster, "A digital fluoroscopic imaging device for radiotherapy localization," Proc. SPIE **1090**, 321–329 (1989).

[35] J. W. Wong, W. R. Binns, A. Cheng, J. W. Epstein, J. Klarmann, M. H. Israel, A. Fenster, and J. A. Purdy, "On-line radiotherapy imaging with an array of fibre-optic image reducers," Int. J. Radiat. Oncol. Biol. Phys. Suppl. 1 **15**, 201 (1988) (Abstract).

[36] J. W. Wong, W. R. Binns, A. Y. Cheng, L. Y. Gear, J. W. Epstein, J. Klarmann, and J. A. Purdy, "On-line radiotherapy imaging with an array of fiber-optic image reducers," Int. J. Rad. Oncol. Bio. Phys. **18**, 1477–1484 (1990).

[37] M. Van Herk and H. Meertens, "A digital imaging system for portal verification," in *Proceedings of the 9th International Conference on the Use of Computers in Radiation Therapy* (Elsevier North-Holland, Amsterdam, 1987), pp. 371–374.

[38] M. Van Herk and H. Meertens, "A matrix ionization chamber imaging device for on-line patient setup verification during radiotherapy," Radiother. Oncol. **11**, 369–378 (1988).

[39] H. Meertens, M. van Herk, J. Bijhold, and H. Bartelink, "First clinical experience with a newly developed electronic portal imaging device," Int. J. Radiat. Oncol. Biol. Phys. **18**, 1173–1181 (1990).

[40] D. F. Anderson and R. A. Holroyd, "High rate operation of a warm-liquid ionization chamber," Nucl. Inst. Meth. A **260**, 343–345 (1987).

[41] R. A. Holroyd and D. F. Anderson, "The physics and chemistry of room temperature liquid-filled ionization chambers," Nucl. Inst. Meth. A **236**, 294–299 (1985).

[42] M. van Herk, "The physics of a liquid filled ionization chamber with pulsed polarizing voltage," in *Conference Records Tenth International Conference on Conduction and Breakdown in Dielectric Liquids*, edited by P. Atten and R. Tobazon, IEEE Cat. No. 90CH2812-6 (IEEE, New York, 1990), pp. 126–130.

[43] M. van Herk, "Physical aspects of a liquid filled ionization chamber with pulsed polarizing voltage," Med. Phys. **18**, 692–702 (1991).

[44] M. G. Albrow *et al.*, "Performance of a uranium/tetramethylpentane electromagnetic calorimeter," Nucl. Inst. Meth. A **265**, 303–318 (1988).

[45] W. F. Schmidt, Can. J. Chem. **55**, 2197–2209 (1977).

[46] J. Engler and H. A. Keim, "A liquid ionization chamber using tetramethylsilane," Nucl. Instrum. Methods. **223**, 47–51 (1984).

[47] A. Gonidec, C. Rubbia, D. Schinzel, and W. F. Schmidt, "Ionization Chambers with Room-Temperature Liquids for Calorimetry," CERN-EP/88-36 (March 1988).

[48] S. Ochsenbein, D. Schinzel, A. Gonidec, and W. F. Schmidt, "Purity in room temperature liquid ionization chambers," Nucl. Instru. Meth. A **273**, 654–656 (1988).

[49] F. J. Bova, L. T. Fitzgerald, W. M. Mauderli, and M. K. Islam, "Real-time megavoltage imaging," Med. Phys. **14**, 707 (1987) (Abstract).

[50] F. Bova, "Recent advances in megavoltage portal imaging and the potential for real-time treatment monitoring," Med. Phys. **15**, 478 (1988).

[51] S. C. Taborsky, W. C. Lam, R. E. Sterner, and G. M. Skarda, "Digital imaging for radiation therapy verification," Opt. Eng. **21**, 888–893 (1982).

[52] K. S. Lam, M. Partowmah, and W. C. Lam, "An on-line electronic portal imaging system for external beam radiotherapy," Brit. J. Radiol. **59**, 1007–1013 (1986).

[53] W. C. Lam, M. Partowmah, D. J. Lee, M. D. Wharam, and K. S. Lam, "On-line measurement of field placement errors in external beam radiotherapy," Brit. J. Radiol. **60**, 361–365 (1987).

[54] G. T. Ewan, "The solid ionization chamber," Nucl. Instr. Meth. **162**, 75–92 (1979).

[55] F. S. Goulding, "Semiconductor detectors—An introduction," IEEE Trans. Nucl. Sci. **NS-25**, 916–920 (1978).

[56] E. J. Morton, W. Swindell, D. G. Lewis, and P. M. Evans, "A linear scintillation-crystal photodiode detector for radiotherapy imaging," Med. Phys. **18**, 681–691 (1991).

[57] J. F. Detko, "Performance characteristics of an ultra-pure germanium gamma camera," Radiology **104**, 431–433 (1972).

[58] L. E. Antonuk, J. Yorkston, J. Boudry, M. L. Longo, J. Jimenez, and R. A. Street, "Development of hydrogenated amorphous silicon sensors for high-energy photon radiotherapy imaging," IEEE Trans. Nucl. Sci. **NS-37**(2), 165–170 (1990).

[59] L. E. Antonuk, J. Boudry, J. Yorkston, C. F. Wild, M. J. Longo, and R. A. Street, "Radiation damage studies of amorphous silicon photodiode sensors for applications in radiotherapy x-ray imaging," Nucl. Instr. Meth. A **299**, 143–146 (1990).

[60] L. E. Antonuk, J. Yorkston, J. Boudry, M. J. Longo, and R. A. Street, "Large area amorphous silicon photodiode arrays for radiotherapy and diagnostic imaging," Nucl. Instr. Meth. A **310**, 460–464 (1991).

[61] IEEE Spectrum, 36–40 (Sept. 1989).

[62] I. D. French, A. J. Snell, P. G. LeComber, and J. H. Stephen, "The effect of gamma-irradiation on amorphous silicon field effect transistors," Appl. Phys. A **31**, 19–32 (1983).

[63] American Association of Physicists in Medicine (AAPM), Rep. No. 24, "Radiotherapy portal imaging quality," Rep. of AAPM Task Group No. 28 (AAPM, New York, 1987).

[64] V. Smith, "Routines for enhancement of radiation therapy images," in *The Use of Computers in Radiation Therapy*, edited by I.A.D. Bruinvis *et al.* (Elsevier, Amsterdam, 1987), pp. 37–40.

[65] G. W. Sherouse, K. Novins, and E. L. Chaney, "Computation of digitally reconstructed radiographs for use in radiotherapy treatment design," Int. J. Radiat. Oncol. Biol. Phys. **18**, 651–658 (1989).

[66] J. Bijhold, K.G.A. Gihuljs, M. van Herk, and H. Meertens, "Radiation field edge detection in portal images," Phys. Med. Biol. **36**, 1705–1710(1991).

[67] K. W. Leszczynski and S. Shalev, "Digital contrast enhancement for on-line portal imaging," Med. Biol. End. Comput. **27**, 507–512 (1989).

[68] K. W. Leszczynski and S. Shalev, "A robust algorithm for contrast enhancement by local histogram modification," Image Vision Comput. **7**, 205–209 (1989).

[69] K. W. Leszczynski and S. Shalev, "An adaptive technique for digital noise suppression in on-line portal imaging," Phys. Med. Biol. **35**, 429–439 (1990).

[70] G. W. Sherouse, J. Rosenman, I. L. McMurry, S. M. Pizer, and E. L. Chaney, "Automatic digital contrast enhancement of radiotherapy films," Int. J. Radiat. Oncol. Biol. Phys. **13**, 801–806 (1987).

[71] H. Meertens, M. van Herk, and J. Weeda, "An inverse filter for digital restoration of portal images," Phys. Med. Biol. **33**, 687–702 (1988).

[72] M. Ishida, H. Kato, K. Doi, and P. H. Frank, "Development of a new digital radiographic image processing system," SPIE Applicat. Opt. Instr. Med. X **347**, 42–48 (1982).

[73] H. Meertens, J. Bijhold, and J. Strackee, "A method for the measurement of field placement errors in digital portal images," Phys. Med. Biol. **35**, 299–323 (1990).

[74] J. Van de Geijn, F. S. Harrington, and B. A. Fraass, "A graticule for evaluation of megavoltage X-ray port films," Int. J. Radiat. Oncol. Biol. Phys. **8**, 1990–2000 (1982).

[75] M. L. Graham, A. Y. Cheng, L. Y. Gear, W. R. Binns, M. W. Vannier, and J. W. Wong, "A method to analyze two-dimensional daily portal images from an on-line fiber-optic imaging system," Int. J. Rad. Oncol. Biol. Phys. **20**, 613–619 (1991).

[76] J. C. Leong and M. A. Stracher, "Visualization of internal motion within a treatment portal during a radiation treatment," Radiother. Oncol. **9**, 153–156 (1987).